44th AIAA Aerospace Sciences Meeting and Exhibit
9 - 12 January 2006, Reno, Nevada

AIAA 2006-299

Comparative advantages of high-order schemes for subsonic, transonic, and supersonic flows

Cosmin Safta,* Kehinde Alabi,† Foluso Ladeinde,‡
Thaerocomp Technical Corporation, P.O. Box 1527, Stony Brook, NY 11790-0609

This computational study aims to verify the order of accuracy of the COMPACT and weighted essentially non-oscillatory (WENO) finite difference schemes implemented in the AEROFLO software, and to identify the comparative advantages of these schemes relative to the low-order (MUSCL-based) schemes for a range of flow problems. The method of manufactured solutions was used to determine the order of accuracy of the spatial differencing schemes. The theoretical sixth-order of accuracy is verified for the COMPACT scheme for subsonic flows, while the theoretical fith-order WENO scheme exhibited a 3.5 order of accuracy for supersonic flows. The MUSCL scheme shows the theoretical second-order accuracy for all flow regimes. The accuracy results were observed for both Cartesian and curvilinear grids. Several subsonic, transonic, and supersonic calculations were then used to evaluate the results from the high- and low-order schemes. For the subsonic and transonic flow configurations, the high-order schemes generally require smaller CPU times, due to their ability to use larger time step sizes or their ability to generate better results with coarser grids as compared to the low-order schemes. For the supersonic flow configurations, both the high- and the low-order schemes capture the shock locations very accurately, although the low-order schemes tend to exhibit significantly larger numerical noise in the regions behind the shocks.

Nomenclature

a,b	=	right hand side parameter for the COMPACT scheme
A, B	=	coefficients for the power-law approximation of the total error
A_R	=	aspect ratio
C_P	=	pressure coefficient
C_L	=	lift coefficient
c	=	chord
c_{rm}	=	coefficients of a Lagrange interpolation (for the WENO scheme)
D	=	diameter
E	=	total energy; total error for the method of manufactured solutions
F, G, H	=	vector of convective fluxes in the physical x, y, and z directions, respectively
F_v, G_v, H_v	=	vector of viscous fluxes in the physical x, y, and z directions, respectively
i,j	=	spatial scheme indices
J	=	Jacobian of the transformation between the physical and the curvilinear coordinate system
M	=	Mach number
p	=	thermodynamic pressure
Q	=	vector of conserved variables
Re	=	Reynolds number
$\widetilde{R}_{Roe}$	=	right eigenvectors matrix of $\partial\hat{F}/\partial Q$ based on a Roe-averaged state at midpoint locations
S	=	source term in the flow conservation equations
St	=	Strouhal number
t	=	time

* Research Engineer, AIAA Member.
† Research Engineer, AIAA Member.
‡ Director of Research, AIAA Life Member and Associate Fellow.

u,v,w	=	velocity components in the physical coordinate system
x,y,z	=	physical coordinate system
α	=	left-hand side parameter for the COMPACT scheme; spectral radius used in the WENO scheme
α_f	=	filter parameter for the compact scheme
γ	=	ratio of specific heats
φ	=	parameter for the Beam-Warming time marching scheme
ϕ	=	generic variable
ρ	=	density
ξ,η,ζ	=	curvilinear coordinate system
ξ_i	=	transformation metrices between the curvilinear and physical coordinate system
Δt	=	time step size
Δ, Δx, Δy	=	grid size
ω	=	vorticity
ω_r , $\tilde{\omega}_r$	=	normalized weights for the WENO scheme

I. Introduction

The vast majority of flows of practical interest exhibit a range of space and time scales that span several orders magnitude. Recent advancement in computing capabilities extended the range of physical phenomena that can be studied through numerical simulations. High-fidelity simulations require an accurate representation of the partial differential equations that describe the physics of the problem of interest. In the past two decades, a large amount of research has been devoted to the use of high-order spatial differencing schemes in computational fluid dynamics. See for example Shu,[20] Visbal and Gaitonde,[21] and the references therein. Unfortunately, the comparative advantages of these schemes over their low-order counterparts have not received enough attention. The aims of the present study are to verify the order of accuracy for several high- and low-order spatial difference schemes and determine the efficiency of high-order schemes for subsonic, transonic, and supersonic flow configurations through comparisons with simulations that use low-order approximations.

The numerical simulations presented in this paper were performed using the AEROFLO software product developed by Thaerocomp Technical Corporation. Several high-order COMPACT[9] and weighted essentially non-oscillatory[20] (WENO) finite difference schemes are considered. Low-order MUSCL-based schemes[8] are also used in the numerical simulations for comparison purposes. Time-integration was performed with either the explicit fourth-order Runge-Kutta algorithm or the second-order implicit Beam-Warming algorithm.[2] In order to accommodate the analysis of realistic problems with complicated geometries and be competitive with unstructured mesh simulations, a matching high-order overset procedure was also developed and implemented.

The method of manufactured solutions (MMS), first proposed by Roache and Steinberg,[13] is a tool for validating codes and identifying their and order of accuracy. Extensive discussions of this method can be found in Salari and Knupp[17] and Roache.[14] For the present study we adopt the methodology of Roy et al.[15] since the parameter set in their study is consistent with our objective to cover all flow regimes.

This paper is organized as follows. The mathematical models and numerical procedures are presented in Section II starting with the flow conservation equations in Section II.A. The spatial and temporal schemes are presented in Sections II.B and II.C, respectively, and the MMS algorithm is described in Section II.D. The discussion of the results is presented in Section III, with the order of accuracy for the spatial discretization schemes reported in Section III.A. Numerical simulations for several configurations of theoretical and practical interest are presented in Section III.B, followed by concluding remarks in Section IV.

II. The Mathematical Models and Numerical Procedures

The transport equations for the flow field variables are presented in this section. The numerical procedures for the spatial and temporal discretization of the transport equations and the implementations of MMS are also presented.

A. The Governing Equations

The fully compressible forms of the continuity, momentum, and energy equations are employed in this study since we are interested in the non-linear coupling between the acoustic and vorticity fields over a wide range of Mach numbers. The conservation equations for the density, $\overline{\rho}$, velocity components, $(\tilde{u},\tilde{v},\tilde{w})$, and the total energy, $\tilde{E}$, in a physical coordinate system (x, y, z) are written in vector form:

$$\frac{\partial Q}{\partial t}+\frac{\partial F}{\partial x}+\frac{\partial G}{\partial y}+\frac{\partial H}{\partial z}=\frac{\partial F_v}{\partial x}+\frac{\partial G_v}{\partial y}+\frac{\partial H_v}{\partial z}+S \tag{1}$$

Here, $Q=\left(\overline{\rho},\overline{\rho u},\overline{\rho v},\overline{\rho w},\overline{\rho E}\right)^T$ is the vector of conserved variables, (F,G,H) are the convective fluxes, (F_v,G_v,H_v) are the viscous fluxes, and S is the source term, which can account for the effects of buoyancy, radiation, and chemical heat release. The expressions for the convective and viscous fluxes, and the source term can be found elsewhere.[1,10,22] Note that an overline on a variable implies Reynolds-averaging, while a tilde denotes Favre-averaging.

A transformation between the physical coordinate system, (x,y,z), and a generalized curvilinear coordinate system, (ξ,η,ς), is introduced to facilitate the numerical simulation of flow configurations around arbitrary complicated bodies. In the curvilinear coordinate system (ξ,η,ζ), Eq. (1) is written as

$$\frac{\partial(Q/J)}{\partial t}+\frac{\partial \hat{F}}{\partial \xi}+\frac{\partial \hat{G}}{\partial \eta}+\frac{\partial \hat{H}}{\partial \zeta}=\frac{\partial \hat{F}_v}{\partial \xi}+\frac{\partial \hat{G}_v}{\partial \eta}+\frac{\partial \hat{H}_v}{\partial \zeta}+\hat{S}\,, \tag{2}$$

where J is the transformation Jacobian. The expressions for the transformed inviscid, $(\hat{F},\hat{G},\hat{H})$, and viscous, $(\hat{F}_v,\hat{G}_v,\hat{H}_v)$, fluxes can be found elsewhere.[1,21] For instance, the convective flux in the computational ξ-direction in Eq. (2) is given by

$$\hat{F}=\frac{1}{J}\left(\xi_x F+\xi_y G+\xi_z H\right), \tag{3}$$

where the ξ_i's are transformation metrices. The transformed source term in Eq. (2) is computed as $\hat{S}=S/J$.

B. Spatial Discretization

Finite differences are used to discretize the convective and diffusive fluxes in Eq. (2). Both low- and high-order spatial differencing schemes are implemented into AEROFLO. These schemes are outlined below.

1. COMPACT

The Padé method is used to approximate the spatial derivatives for subsonic flows. Consider the differencing of a variable ϕ (e.g. conserved variable, flux component, etc.) along the ξ direction, that is $\phi'=\partial\phi/\partial\xi$. An implicit, centered finite difference formula is employed to calculate ϕ':[9]

$$\alpha\phi'_{i-1}+\phi'_i+\alpha\phi'_{i+1}=b\frac{\phi_{i+2}-\phi_{i-2}}{4\Delta\xi}+a\frac{\phi_{i+1}-\phi_{i-1}}{2\Delta\xi}\,. \tag{4}$$

The parameters α, a, and b determine the spatial accuracy of the algorithm and their values are determined using a Taylor series expansion about point i. For a sixth-order accurate scheme, $(\alpha,a,b)=\left(1/3,14/9,1/9\right)$.[6,9]

Compact finite differences are non-dissipative and are susceptible to nonlinear instabilities. In order to remove high frequency noise and maintain solution integrity, a low-pass filtering procedure is adopted. For a typical component of the solution vector, ϕ, the filtered values $\tilde{\phi}$ are obtained from

$$\alpha_f\tilde{\phi}_{i-1}+\tilde{\phi}_i+\alpha_f\tilde{\phi}_{i+1}=\sum_{k=0}^{N}\frac{a_k}{2}\left(\phi_{i+k}+\phi_{i-k}\right). \tag{5}$$

The coefficients a_k are expressed in terms of α_f, which is a parameter that controls the strength of the filter. As α_f is reduced, a wider band of high frequencies is damped. The range $0.3\le\alpha_f<0.5$ has been suggested.[21]

2. WENO

For high-order differencing of flow fields with shock waves at transonic and supersonic Mach numbers, the characteristic-wise weighted essentially non-oscillatory (WENO) procedure is used (see Shu,[20] Procedure 2.10). This numerical approach is summarized below.

Considering the ξ-direction as an example, we have

$$\left.\frac{\partial\hat{F}}{\partial\xi}\right|_i=\frac{1}{\Delta\xi}\left\{\left[\tilde{R}_{Roe}\cdot\left(\tilde{R}_{Roe}^{-1}\cdot\hat{F}\right)\right]_{i+1/2}-\left[\tilde{R}_{Roe}\cdot\left(\tilde{R}_{Roe}^{-1}\cdot\hat{F}\right)\right]_{i-1/2}\right\}, \tag{6}$$

where $\widetilde{R}_{Roe}$ is the matrix formed with the right eigenvectors of the Jacobian $\partial\hat{F}/\partial Q$ computed based on a Roe-averaged state at *i±1/2*. For the characteristic-wise WENO, the reconstruction procedure is performed on the characteristic fields $\hat{F}_c = \widetilde{R}^{-1}_{Roe} \cdot \hat{F}$ to obtain the values at *i±1/2*. The Lax-Friedrichs flux-splitting method is used to obtain the left and right states at the mid-points:

$$\hat{F}^{\pm}_c = \frac{1}{2}\left(\hat{F}_c \pm \alpha q\right), \tag{7}$$

where α is the spectral radius of the Jacobian $\partial\hat{F}/\partial Q$. The characteristic-wise fluxes at the mid-points are reconstructed as

$$\hat{F}^{+}_{c,i+1/2} = \sum_{r=0}^{k-1} \omega_r F^{(r)+}_{c,i+1/2}, \hat{F}^{-}_{c,i+1/2} = \sum_{r=0}^{k-1} \widetilde{\omega}_r F^{(r)-}_{c,i+1/2}, F^{(r)}_{c,i+1/2} = \sum_{m=0}^{k-1} c_{rm} \hat{F}_{c,i-r+m} \ , \tag{8}$$

where ω_r and $\widetilde{\omega}_r$ are normalized weights (see Shu,[20] Section 2.2.2), based on smoothness indicators of the numerical fluxes and c_{rm} are the coefficients of a Lagrange interpolation. Finally, the reconstructed characteristic fluxes are converted back to physical space, $\hat{F}^{\pm}_{i+1/2} = \widetilde{R}_{Roe} \cdot \hat{F}^{\pm}_{c,i+1/2}$, and the numerical flux formed as

$$\hat{F}_{i+1/2} = \hat{F}^{+}_{i+1/2} + \hat{F}^{-}_{i+1/2}. \tag{9}$$

3. MUSCL

A simple low-order scheme is used to assess the performance of the high-order schemes described above. The low-order, yet robust, scheme is based on the MUSCL algorithm introduced by van Leer[6] and extended by Colella and Woodward.[4] First, the left and right values of the primitive variables at mid-point locations are computed as

$$\begin{aligned} \phi_{i+1/2,L} &= \phi_i + \beta_i \Delta_i / 2, \\ \phi_{i+1/2,R} &= \phi_{i+1} - \beta_{i+1} \Delta_i / 2, \end{aligned} \tag{10}$$

where $\phi = (\rho,u,v,w,p)^{\mathrm{T}}$ is the vector of primitive variables, β_i is the limited slope at point *i*, and Δ_i is the grid size. Here, ρ is the density, (u, v, w) are the velocity components, and p is the thermodynamic pressure. The limited slopes β_i are computed using van Leer's harmonic limiter. Based on the left and right states at *i+1/2*, the numerical flux is computed using Roe flux-splitting:[12]

$$\hat{F}_{i+1/2} = \frac{1}{2}\left(\hat{F}_{i+1/2,L} + \hat{F}_{i+1/2,R} - |A|\left(\left(\frac{Q}{J}\right)_R - \left(\frac{Q}{J}\right)_L \right) \right). \tag{11}$$

Here *"R"* and *"L"* values are constructed using the corresponding values of the primitive variables in Eq. (10). Matrix $|A|$ is constructed based on the Roe-averaged state at *i+1/2*, $|A| = R_{Roe}|\Lambda_{Roe}|R^{-1}_{Roe}$, where, $|\Lambda|$ is a diagonal matrix formed with the absolute values of the eigenvalues of the Jacobian $\partial\hat{F}/\partial Q$.

For low-Mach number flows the compact finite differencing scheme is also applied to the viscous fluxes for high-order simulations. When the MUSCL scheme is used to differentiate the convective term, second-order standard finite differences are used to compute the viscous fluxes. For high-Mach number simulations (transonic or supersonic), the viscous effects are small. For this class of flows, the viscous fluxes are also computed based on second-order finite differences.

C. Time Integration

Several time-marching schemes are implemented in AEROFLO. For problems where accurate time-dependent solutions are required, the classical fourth-order Runge-Kutta (RK4) scheme is employed in its low-storage form.[5] For numerical simulations where only the steady state solutions are sought, the stability constraint of the RK4 scheme is found to be too restrictive and it limits the effectiveness of this algorithm. For these problems, the second-order approximate factorization procedure of Beam and Warming[2] with the diagonalized simplification by Pulliam and Chaussee[11] (BW2) is employed in Eq. (12):

$$\left[\left(J^{-1}\right)^{(p+1)}+\frac{1}{1+\varphi}dt\delta_\xi\left(\frac{\partial\hat{F}^{(p)}}{\partial Q}-\frac{\partial\hat{F}_v^{(p)}}{\partial Q}\right)\right]J^{(p+1)}\times$$
$$\left[\left(J^{-1}\right)^{(p+1)}+\frac{1}{1+\varphi}dt\delta_\eta\left(\frac{\partial\hat{G}^{(p)}}{\partial Q}-\frac{\partial\hat{G}_v^{(p)}}{\partial Q}\right)\right]J^{(p+1)}\times \qquad (12)$$
$$\left[\left(J^{-1}\right)^{(p+1)}+\frac{1}{1+\varphi}dt\delta_\zeta\left(\frac{\partial\hat{H}^{(p)}}{\partial Q}-\frac{\partial\hat{H}_v^{(p)}}{\partial Q}\right)\right]\Delta Q=-\frac{dt}{1+\varphi}\left[\begin{array}{l}\left(J^{-1}\right)^{(p+1)}\dfrac{(1+\varphi)Q^{(p)}-(1+2\varphi)Q^{(n)}+\varphi Q^{(n-1)}}{dt}+\\ \delta_\xi\left(\hat{F}^{(p)}-\hat{F}_v^{(p)}\right)+\delta_\xi\left(\hat{G}^{(p)}-\hat{G}_v^{(p)}\right)+\delta_\zeta\left(\hat{H}^{(p)}-\hat{H}_v^{(p)}\right)\end{array}\right]$$

Setting $\varphi=1/2$ in this equation yields a three-point backward stencil in time. Here, derivatives δ_i in the implicit operators on the left-hand side (*lhs*) are computed using standard second-order centered differences, while the right-hand side (*rhs*) differences are computed using the high- and low-order schemes described in Section II.B. In order to reduce the errors associated with the approximate factorization and diagonalization procedure, Newton-like sub-iterations are performed. In Eq. (12) superscript "*n*" correspond to the iteration number, and superscript "*p*" to the sub-iteration number. Within one iteration, $Q^{(p)}=Q^{(n)}$, and as $p\to\infty$, $Q^{(p)}=Q^{(n+1)}$. Typically, three sub-iterations are applied per time step.

D. The Method of Manufactured Solutions

This approach provides a rigorous way to verify the orders of accuracy of the various numerical schemes described in Section II.B. Extensive discussions of this method can be found in Salari and Knupp[17] and Roache.[14] In the present paper we adopt the formulation of Roy et al.[15] since the extension to our code is straight-forward. The MMS procedure is briefly described here.

The steps required to implement the MMS are:

1. Choose the form of the governing equations (include or neglect the viscous fluxes).
2. Assume solutions for the variables (ρ,u,v,w,p), by using analytical functions of interest for these variables. These functions are the manufactured solutions.
3. Substitute the analytical functions in the left-hand side (LHS) of the governing equations, assumed written as $L(\rho^*,u^*,v^*,w^*,p^*)=0$.
4. Write the governing equations as $L(\rho,u,v,w,p)=L(\rho^*,u^*,v^*,w^*,p^*)$, and discretize them using the numerical schemes described in Section II.B.
5. Perform numerical simulations for several grid sizes using analytical boundary conditions and evaluate the order of accuracy of the various spatial differencing schemes.

Step 1. The spatial discretization order is verified for the Navier-Stokes set of equations (see Eq. (2)). Since these equations are discretized for generalized coordinate systems, MMS will be used to verify the accuracy for both Cartesian and curvilinear grids.

Step 2. A two-dimensional configuration is considered in the present study. The assumed solutions for the flow variables are combinations of sine and cosine functions[15]

$$\begin{aligned}\rho(x,y)&=\rho_0+\rho_x\sin\left(\frac{a_{\rho x}\pi x}{L}\right)+\rho_y\cos\left(\frac{a_{\rho y}\pi x}{L}\right)+\rho_{xy}\cos\left(\frac{a_{\rho xy}\pi xy}{L^2}\right)\\ u(x,y)&=u_0+u_x\sin\left(\frac{a_{ux}\pi x}{L}\right)+u_y\cos\left(\frac{a_{uy}\pi x}{L}\right)+u_{xy}\cos\left(\frac{a_{uxy}\pi xy}{L^2}\right)\\ v(x,y)&=v_0+v_x\cos\left(\frac{a_{vx}\pi x}{L}\right)+v_y\sin\left(\frac{a_{vy}\pi x}{L}\right)+v_{xy}\cos\left(\frac{a_{vxy}\pi xy}{L^2}\right)\\ p(x,y)&=p_0+p_x\cos\left(\frac{a_{px}\pi x}{L}\right)+p_y\sin\left(\frac{a_{py}\pi x}{L}\right)+p_{xy}\sin\left(\frac{a_{pxy}\pi xy}{L^2}\right)\end{aligned} \qquad (13)$$

Here, ρ_i, u_i, v_i, and p_i are numerical constants.

Step 3. The analytical functions for the density, velocity components, and pressure shown in Eq. (13) are plugged into Eq. (2) to generate the expressions for the corresponding source terms. In order to minimize the potential for human errors, Mathematica™ symbolic manipulation software is used for this step.
Step 4. Since the source terms do not change for a given computational grid, their values are evaluated in the pre-processing stage to minimize the cost.
Step 5. The exact solution for the flow variables are used as initial conditions and the numerical solution is advanced in time until a quasi-steady-state is reached. In order to determine the order of accuracy, the evolution of the global discretization error is analyzed for several grid sizes. In this study, the L_2 norm is used to define the global discretization error:

$$E = \sqrt{\frac{1}{N_p}\sum_{i=1}^{N_p}\left(\phi_i - \phi_{i,e}\right)^2}\ , \tag{14}$$

where ϕ_i is the numerical value at node i for one of the flow variables, (ρ,u,v,p), $\phi_{i,e}$ is the corresponding exact solution obtained using one of the analytical expressions in Eq. (13), and N_p is the total number of grid points. The least-square method is then used to fit a power-law curve, $E = A(\Delta x)^B$, through the pairs $(\Delta x_k, E_k)$, where Δx_k is the nominal grid space for the computational grid k. The value of coefficient B determines the order of accuracy for a particular numerical scheme, e.g. $B \cong 2$ for a second-order scheme.

III. Results

A. Order of accuracy

The order of accuracy of the MUSCL, COMPACT, and WENO schemes described in the previous section is verified via MMS for Cartesian and curvilinear grids. The Cartesian meshes span unit squares and have uniform grid spacing, $(x,y)_{i,j} = (i-1, j-1)/N$, where $i,j=1,2,\ldots,N+1$, $N = 2^n$, and $n = 3,\ldots,7$. The curvilinear meshes are generated as in Visbal and Gaitonde,[21] by introducing sinusoidal perturbations in the Cartesian grid:

$$x_{i,j} = \frac{i-1}{N} + \alpha \sin\left(a_x \pi \frac{j-1}{N}\right),\ y_{i,j} = \frac{j-1}{N} + \alpha \sin\left(a_y \pi \frac{i-1}{N}\right). \tag{15}$$

In Eq. (15), α controls the strength of the perturbations, while a_x and a_y determine the number of oscillations in the x and y-directions, respectively. For this computational study $a_x = a_y = 3$, and $\alpha = 0.05$, which lead to moderately skewed curvilinear grids. The curvilinear grid corresponding to $N = 64$ is shown in Fig. 1.

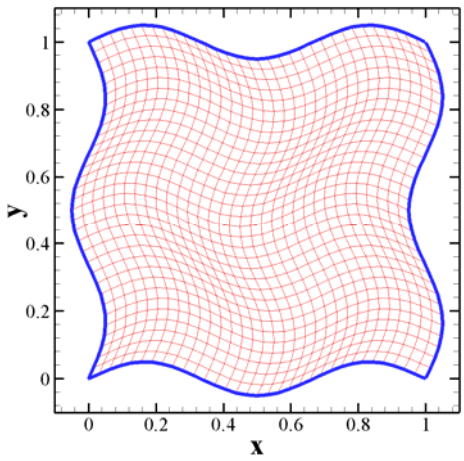

Fig. 1 Curvilinear grid generated using Eq. (15) with $\alpha = 0.05$, $a_x = a_y = 3$, and $N = 64$.

The parameters for the analytical functions for the density, velocity components, and the thermodynamic pressure are similar to the ones used by Roy et al.[15] The parameters for the numerical simulations are given in Table 1. For the subsonic flow regime, the Reynolds number was chosen to ensure that the viscous fluxes in Eq. (1) are of the same order of magnitude as the convective fluxes. For the supersonic flow regime, the viscous fluxes were neglected in the numerical simulations.

Flow Regime	M	Re	Spatial Scheme
Subsonic	0.305	11.4	MUSCL/COMPACT
Supersonic	3.024	-	MUSCL/WENO

Table 1 The parameter set for the numerical simulations used to determine the order of accuracy for the spatial differencing schemes.

1. Subsonic Regime

Sample analytical solutions for the total energy, ρE, are shown in Fig. 2(a) for the subsonic flow simulations at *M=0.305*. Here, E is defined as $E = p/((\gamma-1)\rho) + \left(u^2 + v^2\right)/2$. The source term obtained by plugging the analytical expression for the flow variables in the total energy conservation equation is shown in Fig. 2(b). The values for the Cartesian grid are similar, except the computational domain is a *1x1* square. Several simulations are performed to

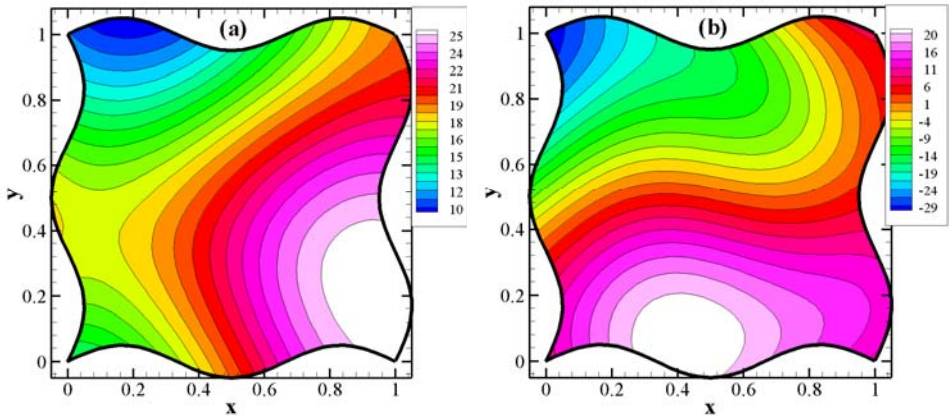

Fig. 2 (a) Total energy, ρE, and (b) total energy transport equation source term for the curvilinear grid shown in Fig. 1**.** The values correspond to the subsonic flow regime simulations.

determine the order of accuracy for COMPACT and MUSCL schemes. For the COMPACT scheme simulations a sixth-order stencil was used for the interior nodes, while at the boundary either a fourth-order or a fifth-order stencil was used. In this section, the results obtained with the fourth-order/sixth-order stencil combination are labeled C_4C_6, while the results obtained with the fifth-order/sixth-order stencil combination are labeled C_5C_6. Sample values corresponding to Cartesian grid simulations are shown in Fig. 3.

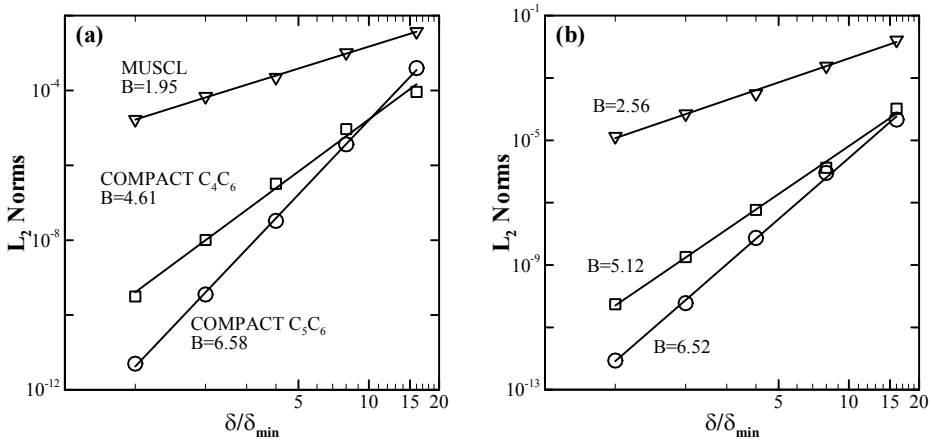

Fig. 3 (a) Density and (b) u-velocity L_2 norms for subsonic simulations on Cartesian grids. Symbols correspond to numerical results and solid lines to power-law least-square fit. The power-law exponent, *B,* is shown for each scheme.

These results confirm the second-order accuracy for the MUSCL scheme. It is interesting to note that, for the COMPACT scheme, a fourth-order stencil at the boundary has a dominant effect on the overall order of accuracy of this scheme, $B \cong 4.75$, while a fifth-order stencil at the boundary does not change the overall sixth order of accuracy. The power coefficient values for all flow variables are given in Table 2. The curvilinear coordinate system has a negligible effect on the order of accuracy for both MUSCL and COMPACT schemes.

Grid Type	Numerical Scheme	Flow Variable			
		ρ	u	v	p
Cartesian	COMPACT C_4C_6	4.61	5.12	4.86	4.54
	COMPACT C_5C_6	6.58	6.52	6.34	6.57
	MUSCL	1.95	2.56	2.38	1.98
Curvilinear	COMPACT C_5C_6	5.68	5.95	6.03	5.90
	MUSCL	2.04	1.82	1.97	1.97

Table 2 Order of accuracy (numerical values for the power coefficient, B) for the COMPACT and MUSCL schemes corresponding to subsonic simulations.

2. Supersonic Regime

Sample analytical solutions for the total energy, ρE, are shown in Fig. 4(a) for the supersonic flow simulations. Although these solutions correspond to a Mach number $M=3$, no shocks are observed since the manufactured values

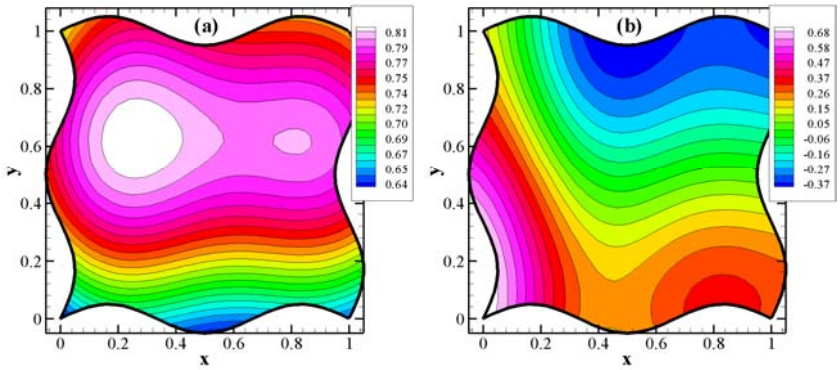

Fig. 4 (a) Total energy, ρE, and (b) total energy transport equation source term for the curvilinear grid shown in Fig. 1**.** The values correspond to the supersonic flow regime simulations.

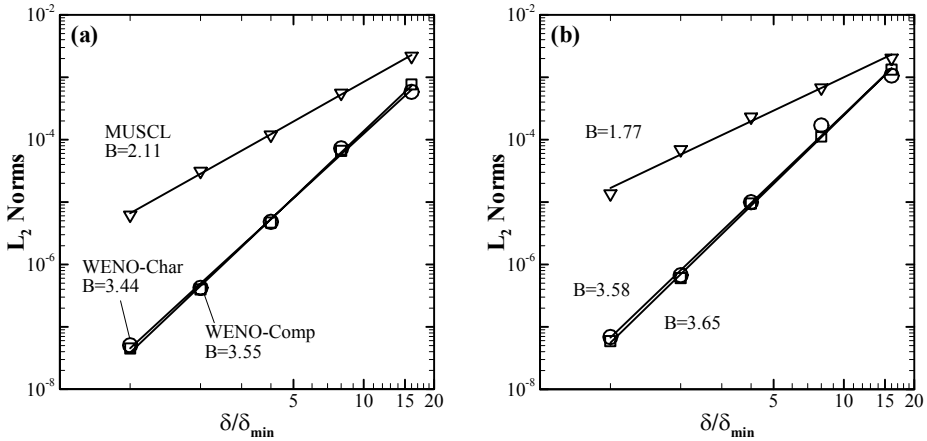

Fig. 5 (a) Pressure and (b) v-velocity L_2 norms for supersonic simulations on curvilinear grids. Symbols correspond to numerical results and solid lines to power-law least-square fit. The power-law exponent, B, is shown for each scheme.

are smooth. The equivalent source term is shown in Fig. 4(b). The values for the Cartesian grid are similar, except the computational domain is a *1x1* square. Several simulations are performed to determine the order of accuracy for WENO and MUSCL schemes. Both the characteristic-wise and component-wise reconstruction algorithms were used in the WENO scheme. Sample values corresponding to curvilinear grid simulations are shown in Fig. 5.

The MUSCL scheme retains the second-order accuracy for the supersonic flow regime. Both variants of the WENO scheme exhibit a superior order of accuracy, the values for the power coefficient are between 3 and 4. The power coefficient values for all flow variables are given in Table 3.

Grid Type	Numerical Scheme	Flow Variable			
		ρ	u	v	p
Cartesian	WENO-char	3.52	3.84	3.56	3.23
	MUSCL	1.96	2.04	1.93	2.04
Curvilinear	WENO-char	3.52	3.60	3.58	3.44
	WENO-comp	3.51	3.65	3.65	3.55
	MUSCL	1.77	1.97	1.77	2.11

Table 3 Order of accuracy (numerical values for the power coefficient, *B*) for the WENO and MUSCL schemes corresponding to supersonic simulations.

Similar to the subsonic regimes, the order of accuracy values for MUSCL and WENO are not affected by the curvilinear grids system compared to the Cartesian meshes.

B. Comparative advantages of high-order schemes

The parameter set for the cases investigated are shown in Table 4 below. For all simulations involving the flow over a cylinder, subsonic and supersonic, the Reynolds number (*Re*) was set small enough in order to enforce a laminar solution.

Flow Regime	Configuration	Ma	Re	Time integration
Subsonic	Cylinder	0.2	150	RK4
	NACA0012	0.3	$6*10^6$	BW2
Transonic	NACA0012	0.84	$9*10^6$	BW2
	ONERA M6 wing	0.84	-	BW2
Supersonic	Cylinder	1.5/3.0	$2*10^2$	BW2
	Forward-Facing Step	3.0	-	RK4

Table 4 Parameter set for the simulations selected for comparison

For the simulations involving the flow over the NACA0012 airfoil, the Reynolds numbers were set to match the experimental conditions. For these simulations, the Spalart-Allmaras one-equation turbulence model[19] was used to compute the eddy viscosity. The flow over the ONERA M6 wing and the flow over the forward-facing step were computed using the Euler set of equations.

1. Subsonic Regime - Flow over a cylinder

For the flow over a cylinder, the computational mesh consists of $N_\xi \times N_\eta = 201 \times 78$ grid points. Here, the ξ-direction runs clockwise around the cylinder starting from the leading edge, while the η-direction runs radial from the cylinder surface to the outer edge of the computational domain, which is a circle of radius *R/D=50*, where *D* is the diameter of the cylinder. Fig. 6 shows a detail of the computational mesh near the cylinder. The radial grid lines are clustered near the cylinder, $\delta_{min}=0.002$, in order to accurately capture the laminar boundary layer that forms near the wall.

Since lower order methods were also proven to capture well the flow physics for this problem, the number of grid nodes was deliberately kept low, to highlight the computational advantage of higher-order methods. For all simulations, the initial streamwise velocity was set to the reference value, the crosswise component was set to zero, while the density and pressure were also set to their reference values. Numerical tests showed that a computational

time step size of $\Delta t = 6\times10^{-4}$ is sufficient for COMPACT to capture the time dependent solutions, while for the

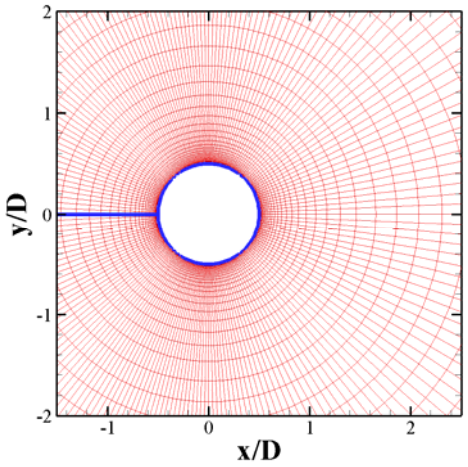

Fig. 6 Computational mesh around the cylinder for subsonic flow simulations at *M=0.2* and *Re=150*.

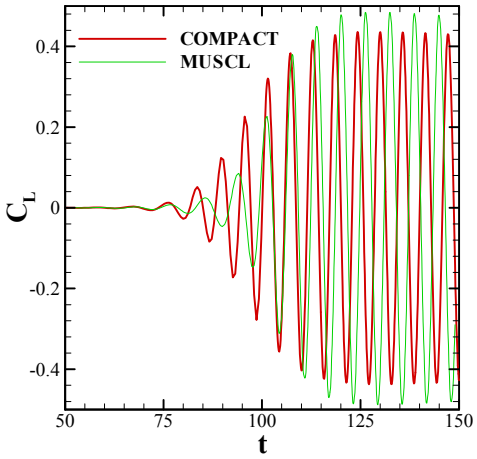

Fig. 7 Time evolution of the lift coefficient for the flow over a cylinder.

MUSCL scheme the time step needed to be halved, $\Delta t = 3\times10^{-4}$, to obtain stable simulations.

The vortex shedding pattern characteristic for this configuration starts at approximately *t=75*. The time dependent lift coefficient, shown in Fig. 7, is used to compute the Strouhal number, *St*, for the two computational schemes. For the COMPACT scheme *St=0.174*, which is in good agreement with the experimental range of 0.178-0.187 presented in Roshko.[16] The MUSCL scheme predicts a lower value, *St=0.16*.

The vorticity field predicted by the COMPACT scheme, in Fig. 8(a), exhibits well defined vortices even for *x/D>10* where the computational grid becomes coarse. The results obtained with MUSCL scheme, in Fig. 8(b), are in qualitative agreement with the COMPACT results for *x/D<5*, where the computational grid is relatively dense. At locations further downstream where the grid becomes coarse, the vortices are dissipated fast by the lower-order scheme.

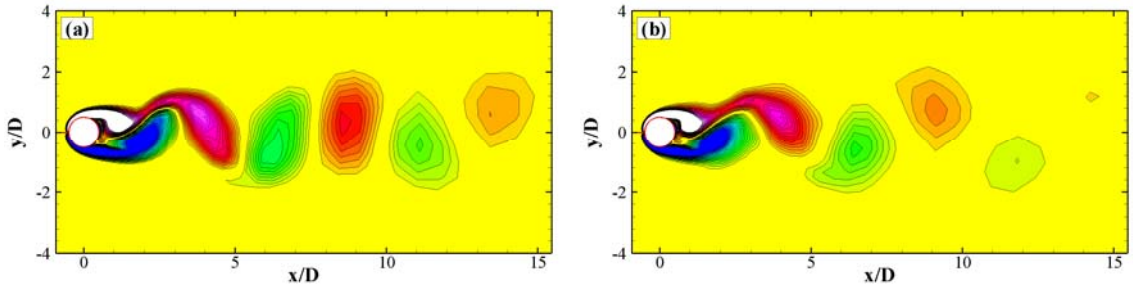

Fig. 8 Instantaneous vorticity contours for (a) COMPACT and (b) MUSCL schemes for flow over a cylinder at Re=150, Ma=0.2. The scale of the vorticity contours is the same in both subplots.

2. Subsonic Regime - Flow over NACA0012

The conditions for Mach and Reynolds numbers for the simulation around the NACA0012 airfoil matched the experimental conditions presented in Harris.[7] The angle of attack was set to $\alpha = 9.86^o$. At $M = 0.3$ the compressibility effects are still small enough such that the flow around the airfoil is free of discontinuities.

Several O-type computational grids, generated with GRIDGEN software, were considered for this configuration. The characteristics for these grids are summarized in Table 5. The grid refinement increases from mesh *M1* (coarse grid) to mesh *M3* (fine grid).

Mesh	M1	M2	M3
N_ξ	127	187	245
$N_{\xi,TE}$	6	8	10
A_R	1.111	1.085	1.070

Table 5 Characteristics of the O-type computational grids around the NACA0012 airfoil

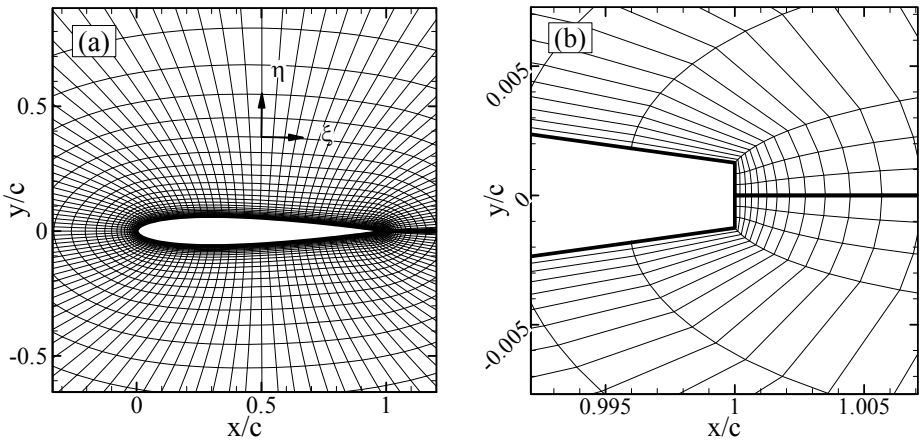

Fig. 9 Close-up view of mesh M1: (a) around the airfoil, and (b) near the trailing edge. The outer boundary of the mesh is a circle of radius *R/c=50*, centered at the origin. Here, *c* is the airfoil chord.

The grid lines/points were clustered near the airfoil, particularly near the leading and trailing edges. Close-up views for mesh M1 are also shown in Fig. 9. In Table 5, N_ξ is the number of points in the computational ξ–direction which runs clockwise around the airfoil starting from the trailing edge; $N_{\xi,TE}$ is the number of points at the trailing edge, and A_R is the compression factor near the leading edge of the airfoil. For all meshes, $N_\eta=50$, where η is the computational direction running radial from the airfoil to the free stream.

A parametric study was performed to optimize the values of the time step sizes for each numerical scheme. For WENO simulations, it was found that a value of $\Delta t=2\times10^{-4}$ was sufficient to obtain a steady-state solution. For MUSCL, this time step size led to an oscillatory behavior of the pressure field in the boundary layer around the airfoil and resulted in a "jagged" profile of the pressure coefficient, C_p (Fig. 10). These oscillations were significantly reduced (although not entirely eliminated) for MUSCL scheme simulations using a value of $\Delta t=1\times10^{-4}$.

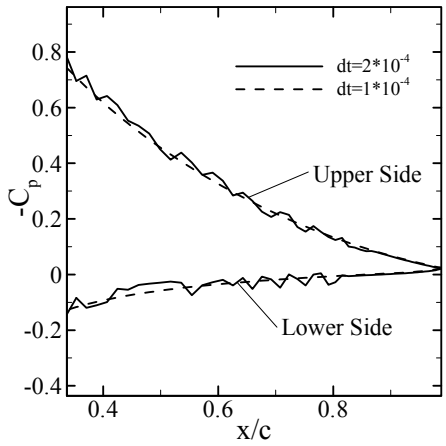

Fig. 10 The pressure coefficient for MUSCL scheme and mesh M3.

The required computational time step size for the COMPACT scheme (Fig. 11) was found to be similar to that for WENO. A parametric study was also performed for the COMPACT scheme to determine the effect of the filtering scheme parameter α_f, (Section II.B.1) on the results. Sample C_P results are shown in Fig. 12. These simulations were performed with mesh M3 and a computational time step size of $\Delta t=2\times10^{-4}$. For $\alpha_f=0.4$, the C_P profile exhibit oscillations near the leading and trailing edges of the airfoil, while for $\alpha_f=0.35$ the results are smooth. A further reduction in the value of α_f had negligible effect on the solution.

Table 6 summarizes the time step size, CPU times, and the number of iterations for the three schemes. Although MUSCL is the least expensive per computational time step compared to the COMPACT and WENO schemes, it requires more CPU time, due to smaller time step size.

The pressure coefficient results, shown in Fig. 13, are close to the experimental results for all spatial discretization schemes except for a small region near the trailing edge. Fig. 14 shows the C_P profile for the upper side of the airfoil near the leading edge. The WENO results obtained on coarse (M1) and fine (M3) meshes are in good agreement and close to the experimental data. For the COMPACT scheme, the results are approximately 7% smaller compared to the experimental values. The C_p values for the MUSCL scheme (results not shown) are approximately 10-15% smaller compared to the experimental values near the leading edge of the airfoil.

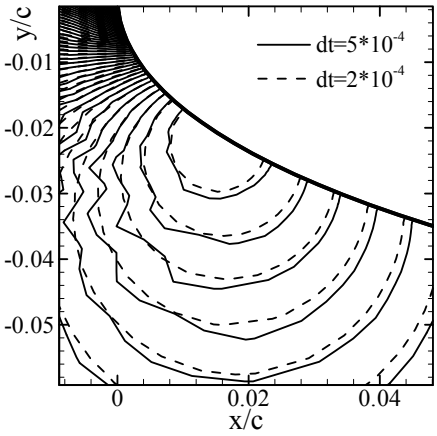

Fig. 11 Pressure field contour plots for COMPACT scheme using Mesh M3.

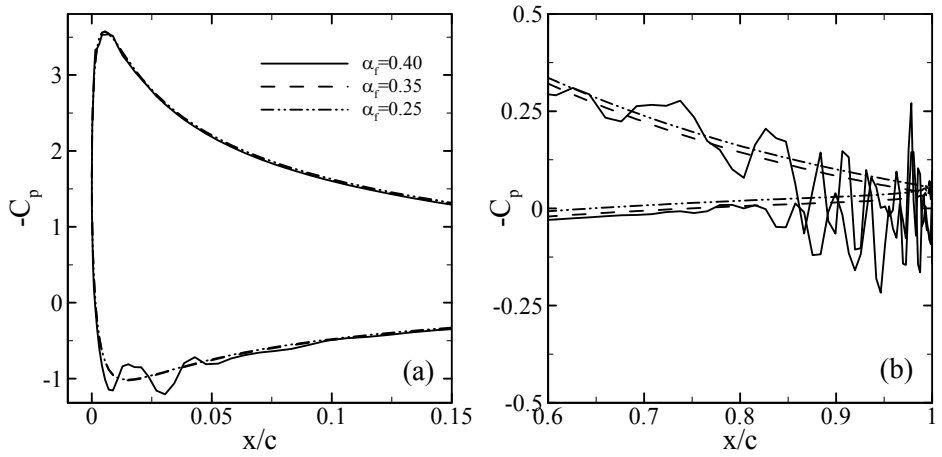

Fig. 12 (a) Leading edge and (b) trailing edge details of the pressure coefficient for subsonic flow over NACA0012 obtained with COMPACT scheme using Mesh M3 and various values of filter parameter α_f.

Scheme	Time Step	CPU time	No. of iterations
WENO	2×10^{-4}	1.0	100×10^{3}
MUSCL	1×10^{-4}	1.5	200×10^{3}
COMPACT	2×10^{-4}	0.79	100×10^{3}

Table 6. Time step size, CPU time, and number of iterations for simulations corresponding to mesh M3 for subsonic flow over NACA0012. The CPU times are normalized with the value for the WENO scheme.

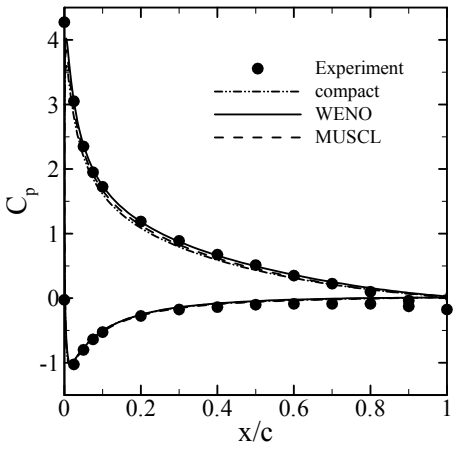

Fig. 13 Comparison between experimental and computational results for the pressure coefficient obtained with mesh M3 for subsonic flow over NACA0012.

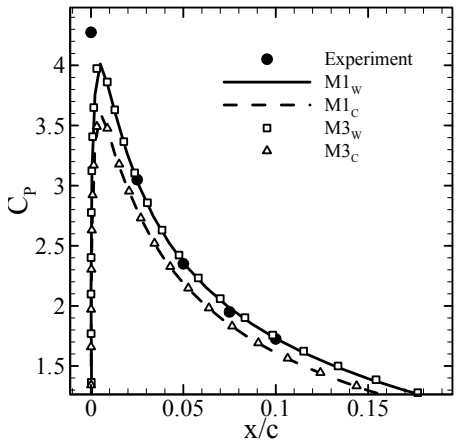

Fig. 14 Comparison between experimental and computational results using WENO (subscript W) and COMPACT (subscript C) for the pressure coefficient obtained with M1 and M3. Results correspond to the same flow conditions as in Fig. 13.

The velocity fields for WENO and COMPACT schemes are compared in Fig. 15. Although there are no experimental or computational data available for comparison, it appears that WENO provides a better approximation of the flow field on the upper side of the airfoil where boundary layer separation occurs. As mentioned above, the results for the COMPACT scheme are independent of the value used for the filtering parameter.

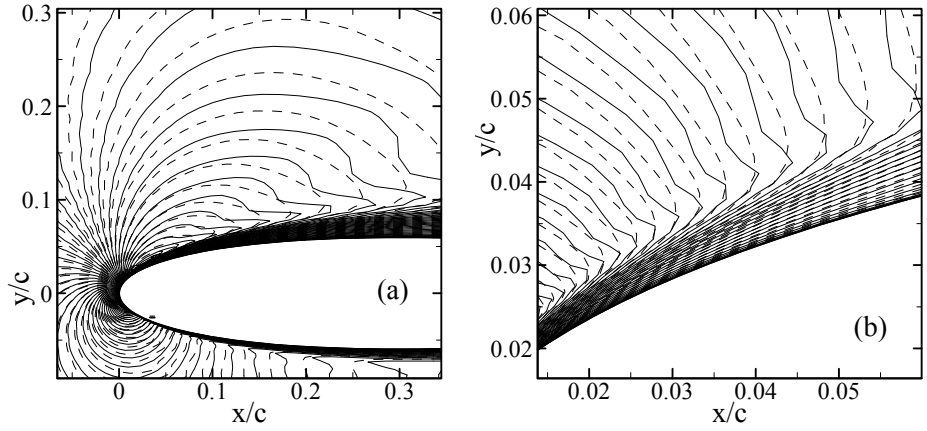

Fig. 15 (a) u-velocity and (b) v-velocity contour plots for numerical simulations using WENO (dashed line) and COMPACT (solid line) with mesh M3. Results correspond to the same flow conditions as in Fig. 13.

3. Transonic Regime - Flow over NACA0012

For this case, the angle of attack was set to $\alpha = 2.86^o$ to match one of the experiments in Ref. [7]. The conditions for this case lead to the formation of a shock wave on the upper side of the airfoil at $x/c \cong 0.5$. For this study, the computational grids are the same as for the subsonic flow simulations presented in Section III.B.2.

Table 7 lists the computational times for each mesh and numerical scheme used in the numerical simulations. For all simulations, the time step was fixed at $\Delta t = 5 \times 10^{-4}$. It was found that larger time steps led to unacceptable results, irrespective of the numerical scheme used. For the same mesh size, WENO scheme is the most expensive for the same grid size, with a CPU time approximately 50% larger than MUSCL. The relative computational time for COMPACT scheme varies with the number of grid points, and for the largest mesh, M3, it becomes close to WENO.

Mesh	CPU time ratio			
	WENO/MUSCL	WENO/COMP	WENO (M1)/MUSCL	WENO (M1)/COMP
M1	1.44	1.28	1.44	1.28
M2	1.49	1.24	0.97	0.81
M3	1.47	1.11	0.74	0.55

Table 7 CPU Time comparison for simulations of transonic flow over NACA0012. For all simulations the CPU time corresponds to *40,000* time steps or *t=20***.**

The pressure coefficient results, shown in Fig. 16 indicate that WENO results are closer to the experimental data on the upper surface of the airfoil (top lines and symbols) compared to the other two schemes. On the lower surface, the numerical results agree well with each other. The pressure field contour lines are further examined in Fig. 17 to identify the similarities and differences between the finite difference schemes. The pressure field results for WENO and MUSCL shown in Fig. 17 (a) are close and the topology is similar to other published computational results.[24] The contour lines for COMPACT in Fig. 17 (b) are jagged near the shock wave on the upper surface of the airfoil. These results are independent of the computational time step size used. Simulations were also performed using smaller time step sizes with similar outcome. These differences support the well known fact that the COMPACT scheme is less appropriate for transonic flow simulations.

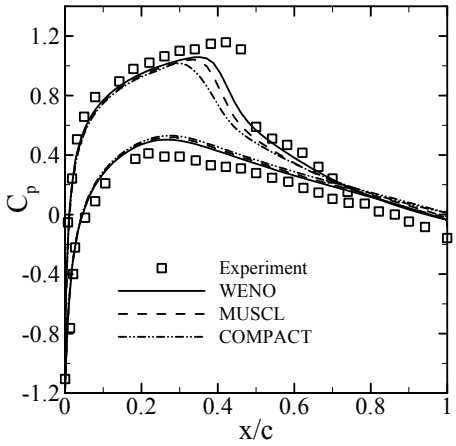

Fig. 16 Comparison between experimental and computational results for the pressure coefficient obtained with mesh M3 for transonic flow over NACA0012.

The results for WENO and MUSCL obtained on meshes M1 and M3 are compared in Fig. 18 to determine their relative performance. Data obtained with WENO on mesh M3 is used as a base for comparison since these results are closer to the experimental data. The C_P profiles show that the WENO scheme with mesh M1 generates better results than MUSCL on the finer mesh M3. Therefore, WENO is the most computationally efficient scheme to capture the transonic flow characteristics.

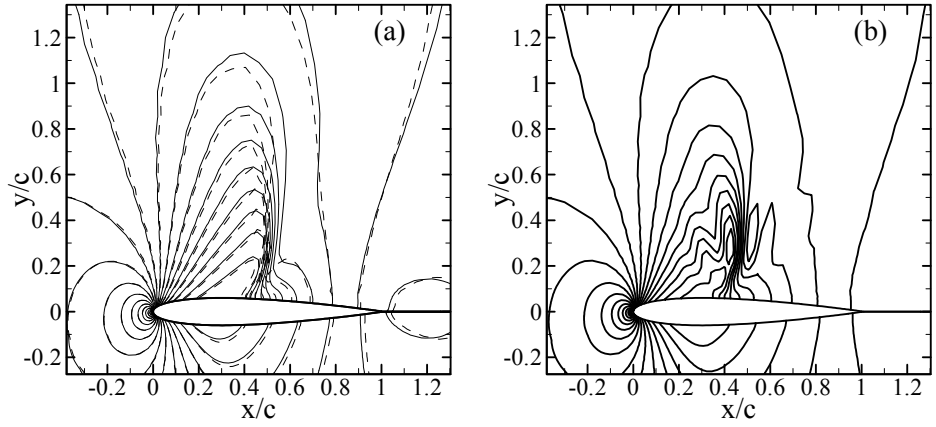

Fig. 17 Pressure field contour lines for (a) WENO (solid lines), MUSCL (dashed lines), and (b) COMPACT obtained with mesh M3. Results correspond to the same flow conditions as in Fig. 16.

4. Transonic Regime – Flow over ONERA M6 Wing

This configuration is a classical validation problem[18] because of the simple geometry combined with the complexity of the transonic flow pattern. The 3-block Euler grid used in the numerical simulations is a combination of two large H-H grids, for the upper and lower sides of the wing, respectively, and a smaller C-type grid for a better solution near the leading edge of the wing: upper side of wing (99×57×33=182457), lower side of wing (99×57×33=182457), and leading edge patch (41×45×22=40590). This results in a total of 413,000 grid points. The normal grid spacing near the wing is 5×10^{-3}. An composite view of the computational blocks is shown in Fig. 19(a). The distribution of grid lines on the surface of the wing is shown in Fig. 19(b).

The parameters for the numerical simulations are set to match the experimental conditions.[18] The

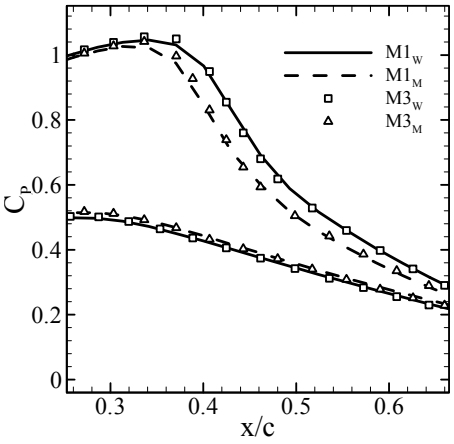

Fig. 18 Pressure coefficient comparison between WENO (subscript W) and MUSCL (subscript M) obtained with meshes M1 and M3.

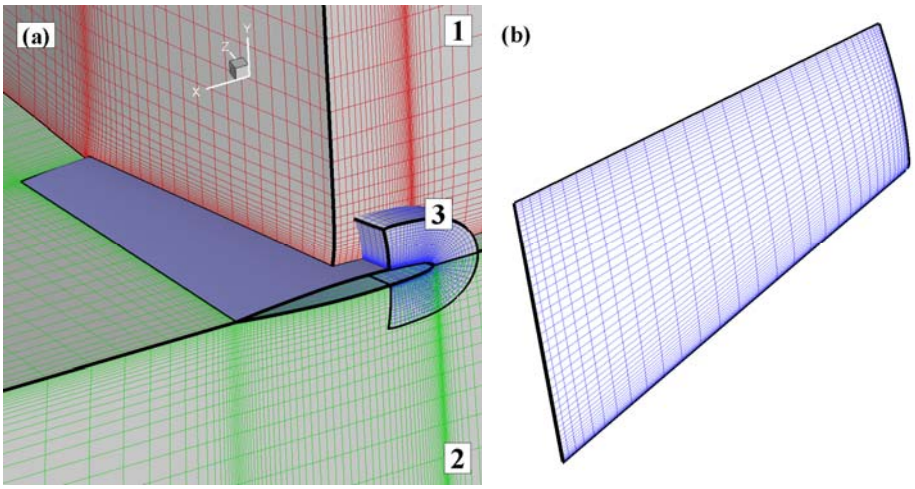

Fig. 19 Computational grid around ONERA M6 wing: (a) composite view of the three computational blocks (some of the grid planes were eliminated from Block 1 to enhance the view), and (b) computational grid on the wing surface.

gradient of pressure is zero while the density and velocities are prescribed at the inflow. The streamwise and transverse velocity components were set to match the reference Mach number and angle of attack. At all other external boundaries, zero-gradient conditions were prescribed for all variables, except the pressure, which is imposed at the outlet. The interface between Blocks 1 and 2 conform, which allows a natural extension of the computational scheme across this boundary without loss of accuracy. Slip wall conditions were imposed at the wing surface. The converged results for pressure, obtained with the WENO scheme, are shown in Fig. 20. These results show the existence of two compression waves on the upper side of the wing, in agreement with the experimental observations. Examination of the pressure contours in the overset region (see leading edge of the wing in the symmetry plane) reveals a smooth transition across the boundaries between the overset blocks.

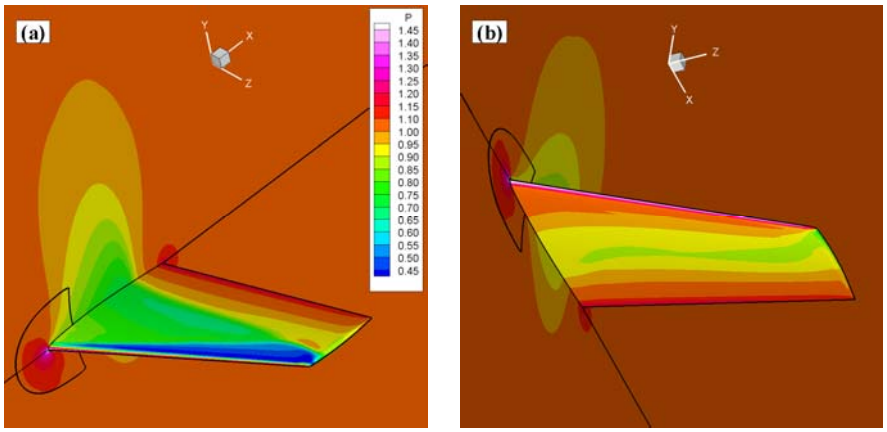

Fig. 20 Pressure contours on the wing surface and the symmetry plane obtained using the WENO scheme: (a) upper side view and (b) lower side view. The boundaries of the computational blocks are shown with black lines.

In order to assess the performance of the WENO and MUSCL schemes for this problem, the profiles of the pressure coefficient are compared with the experimental data at various locations across the wing span in Fig. 21. It can be observed that WENO results compare well at all locations. The MUSCL results are also close to the experiments, although the shock locations are captured less accurately compared to WENO.

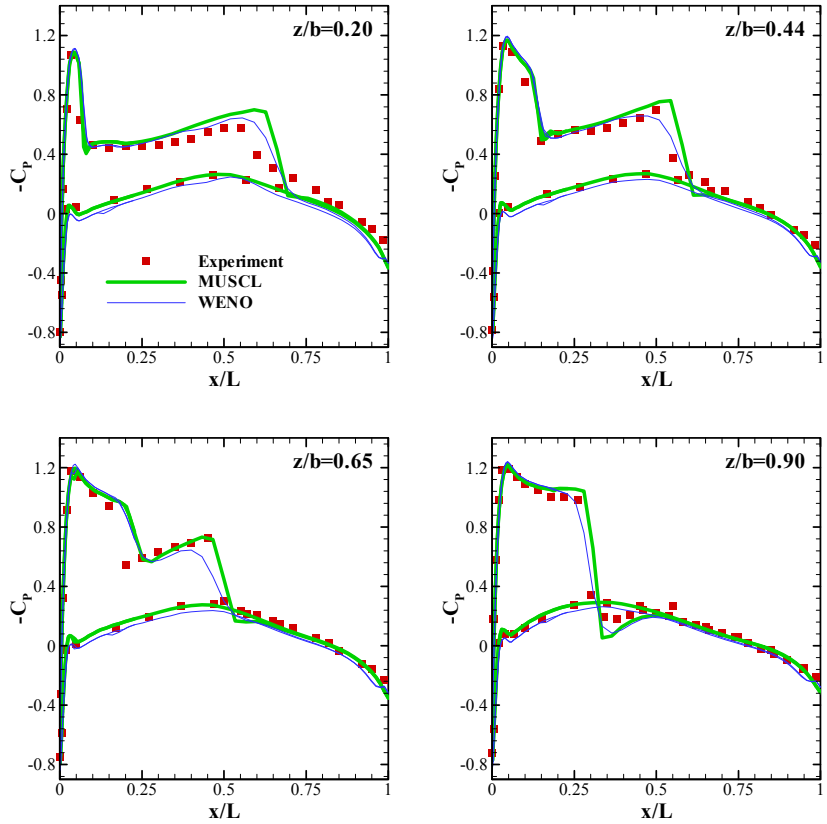

Fig. 21 Comparison of numerical (solid lines) and experimental (symbols) results for the pressure coefficient at various locations across the wing span.

5. Supersonic Regime – Flow over a Cylinder

The computational grid around the cylinder for the supersonic flow calculations is similar to the one used for the subsonic flow simulations presented in Section III.B.1. Although realistic conditions for this problem require larger Reynolds numbers than the ones shown in Table 4, we adopted artificially small values to relax the constraint of small grid spaces near the cylinder wall, and eliminate the need for turbulence modeling.

Fig. 22(a) shows the Mach number contours obtained with WENO for the case with reference *M=1.5*. In this figure, the thick solid line corresponds to the experimental shock location constructed using the experimental correlations given by Billig.[3] The WENO scheme generates smooth results and the upstream shock location and shape is in good agreement with the experiments. After the bow shock, the flow undergoes a supersonic expansion as it passes the vertical axis through the center of the cylinder. A secondary oblique shock is observed in the wake of the cylinder as the flow regains its horizontal orientation. Fig. 22(b) shows the MUSCL results for the same conditions as in Fig. 22(a). Although the shock location for the MUSCL scheme is similar to the one obtained with WENO, the low-order scheme exhibits "jagged" Mach number contours compared to the high-order scheme. Similar behavior was also observed for the other flow variables (results not shown).

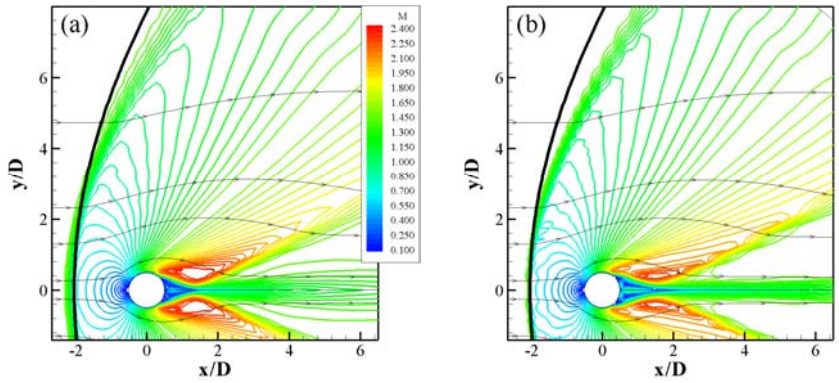

Fig. 22 Mach number contours for (a) WENO and (b) MUSCL schemes for flow around a cylinder at *M=1.5*.

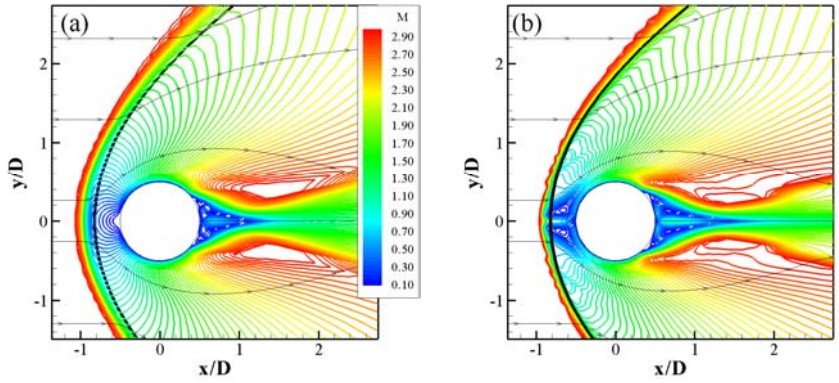

Fig. 23 Mach number contours for (a) WENO and (b) MUSCL schemes for flow around a cylinder at *M=3*.

The WENO scheme results remain smooth as the reference Mach number is increased to *M=3.0*, in Fig. 23. For this case, the quality of the results obtained with MUSCL is further degraded compared to that for WENO results, especially in the region upstream of the cylinder and downstream of the bow shock.

6. Supersonic Regime – Forward – Facing Step

This is a classical test problem (see the review article by Woodward and Colella[23] and the references therein). More recently, this configuration was used by Shu[20] to demonstrate the ability of the WENO scheme to capture the shock patterns.

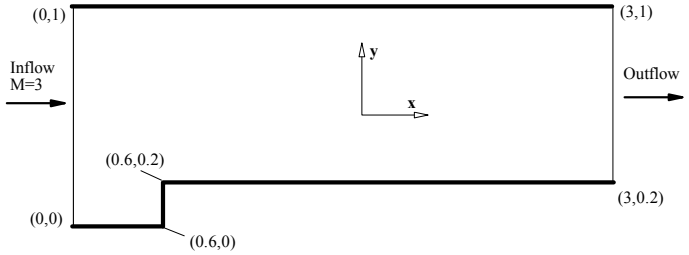

Fig. 24 Schematic of the forward-facing step configuration. The normalized coordinates for relevant locations are shown in this sketch.

A schematic of the physical domain is shown in Fig. 24. Inflow boundary conditions are imposed at the left boundary while, at the right boundary, the gradients are assumed to be zero for all flow variables. Since the flow is supersonic at the right boundary, the Neumann boundary condition has no effect on the flow upstream. Slip-wall conditions are applied at the bottom and top boundaries. The corner at (0.6,0.2) is the center of a rarefaction fan and is a singular point. Woodward and Colella[23] adopted a special treatment for the flow solution at the grid points near this corner, in order to eliminate the artificial boundary layer that develops on the bottom wall. Since the objective of our study is to compare the quality of the low- and high-order schemes, no special treatments were used for the grid points near the singularity point.

MUSCL and WENO simulations are performed using a Cartesian grid with $\Delta x = \Delta y = 1/80$, which results in 241x81 grid points. These results compare well with previous calculations,[20] except for the interaction between the oblique shocks and the boundary layer that develops on the bottom wall. Although the MUSCL results compare qualitatively well compared to those for WENO, in the shock regions they show larger amplitudes for the numerical noise compared to the higher-order scheme.

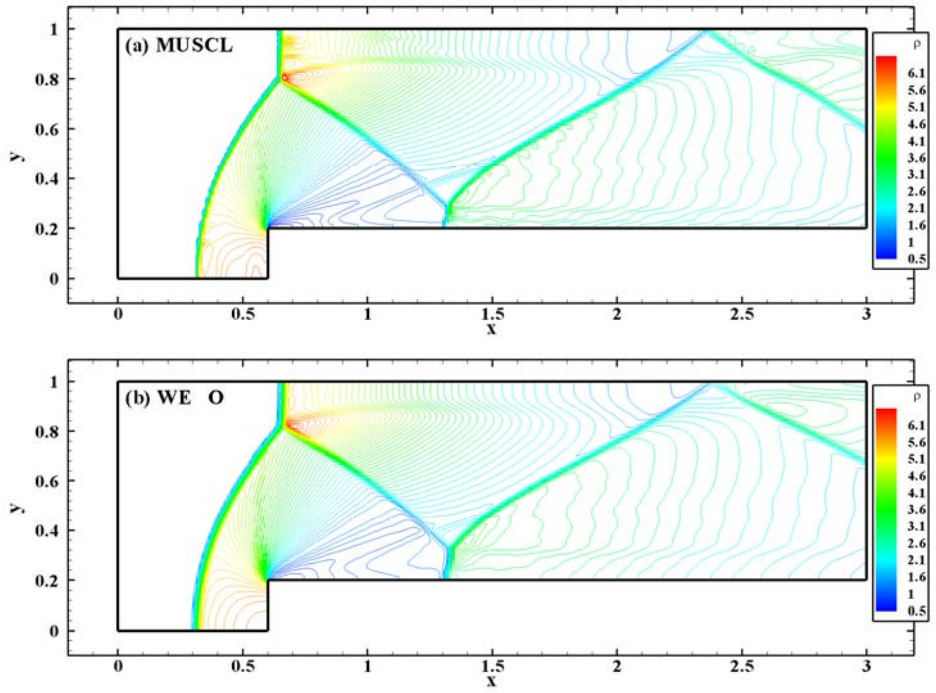

Fig. 25 Density contours for the *M=3* forward-facing step problem at *t=4* obtained with (a) MUSCL and (b) WENO.

IV. Conclusions

The main objectives of the present study are to verify the order of accuracy of several spatial discretization techniques implemented in the AEROFLO software, and to determine the potential advantages the high-order schemes over their low-order counterparts in capturing the flow physics for all flow regimes.

The first objective was achieved via the method of manufactured solutions (MMS). Using this approach, a second-order accuracy was demonstrated for the MUSCL scheme for all flow regimes. The theoretical sixth-order of accuracy is verified for the COMPACT scheme for subsonic flow conditions. It was found that a fifth-order stencil at the boundary did not affect the overall order of the sixth-order COMPACT. For the supersonic flow regime the theoretical fifth-order WENO scheme provided a 3.5 order of accuracy for all flow variables. The observed orders of accuracy were similar for both the Cartesian and curvilinear grids.

Several subsonic, transonic, and supersonic configurations of theoretical and practical interest were considered to achieve the second objective. The superiority of high-order schemes over the low-order schemes is also verified through comparisons with experimental data wherever available. The main results from this study can be summarized as follows:

Subsonic flow

1. At small Mach numbers (*M=0.2*), the COMPACT scheme is the most efficient and leads to accurate vortex shedding frequency for the flow around the cylinder even for relatively coarse grids.
2. The low-order MUSCL scheme is more dissipative and the vortex shedding pattern is compromised for the same computational grids as for COMPACT. Moreover the total CPU time for the MUSCL scheme is larger compared to that for COMPACT since the computational time step is smaller.
3. For larger but still subsonic Mach numbers, WENO becomes more accurate than COMPACT, and its results replicate the experimental values for the flow around NACA0012 airfoil at M=0.3.

Transonic flow

4. The WENO scheme provides better results for the shock location on the upper surface of the NACA 0012 airfoil, and is more efficient, requiring approximately 26% less CPU time relative to MUSCL. WENO generates more accurate results using a fewer number of grid points.
5. For the same grid size the shock locations for the flow over the ONERA M6 wing are more accurately calculated by WENO compared to MUSCL.

Supersonic flow

6. Both WENO and MUSCL schemes provide a good approximation for the shock wave location for the flow over the cylinder and the flow over a forward-facing step.
7. For the same computational grid, the WENO results are considerably smoother compared to the results for MUSCL, particularly in the flow regions behind the shocks.

Acknowledgments

This work was funded by the United States Air Force, Contracts F33615-03-C-3315 and FA8650-04-C-2496, via the Phase II SBIR Program. The authors are very grateful to the Air Force for giving Thaerocomp the opportunity to develop innovative research tools for high-performance numerical simulations.

References

[1] Anderson, D. A., Tannehill, J. C., and Pletcher, R. H., *Computational Fluid Mechanics and Heat Transfer*, McGraw-Hill, New York, 1984.

[2] Beam, R. M., and Warming, R. F., "An Implicit Factored Scheme for the Compressible Navier-Stokes Equations," *AIAA Journal*, Vol. 16, No. 4, 1978, pp. 393-402.

[3] Billig, F.S., "Shock-Wave Shapes around Spherical- and Cylindrical-Nosed Bodies," *Journal of Spacecraft and Rockets*, Vol. 4, No. 6, 1967, pp. 822-823.

[4] Colella, P., and Woodward, P. R., "The Piecewise Parabolic Method (PPM) for Gas-Dynamical Simulations," *Journal of Computational Physics*, Vol. 54, 1984, pp. 174-201.

[5] Fye, D. J., "Economical Evaluation of Runge-Kutta Formulae," *Mathematics of Computation*, Vol. 20, No. 95, 1966, pp. 392-398.

[6] Gaitonde, D. and Visbal, M., "High-Order Schemes for Navier-Stokes Equations: Algorithm and Implementation into FDL3DI," Technical Report AFRL-VA-WP-TR-1998-3060, Air Force Research Laboratory, Wright-Patterson AFB, 1998.

[7] Harris, C. D., "Two-dimensional Aerodynamic Characteristics of the NACA0012 Airfoil in the Langley 8-Foot Transonic Pressure Tunnel," NASA TM 81927, 1981.

[8] Van Leer, B., "Towards the Ultimate Conservative Difference Scheme V. A Second-Order Sequel to Godunov's Method," *Journal of Computational Physics*, Vol. 32, 1979, pp. 101-136.

[9] Lele, S. K., "Compact Finite Differences with Spectral-Like Resolution," *Journal of Computational Physics,* Vol. 103, No. 1, 1992, pp. 16-42.
[10] Pope, S.B., *Turbulent Flows*, Cambridge University Press, 2000.
[11] Pulliam, T. H., and Chaussee, D. S., "A Diagonal Form of an Implicit Approximate-Factorization Algorithm," *Journal of Computational Physics*, Vol. 39, No. 2, 1981, pp. 347-363.
[12] Roe, P.L., "Characteristic-Based Schemes for the Euler Equations," *Annual Review of Fluid Mechanics*, Vol. 18, 1986, pp. 337-365.
[13] Roache, P.J., and Steinberg, S., "Symbolic manipulation and Computational Fluid Dynamics," *AIAA Journal*, Vol. 22, No. 10, 1984, pp. 1390-1394.
[14] Roache, P.J., "Code Verification by the Method of Manufactured Solutions," *Journal of Fluids Engineering*, Vol. 124, No. 1, 2002, pp. 4-10.
[15] Roy, C.J., Nelson, C.C., Smith, T.M., and Ober, C.C., "Verification of Euler/Navier-Stokes Codes using the Method of Manufactured Solutions," *International Journal for Numerical Methods in Fluids*, Vol. 44, 2004, pp. 599-620.
[16] Roshko, A., "On the Development of Turbulent Wakes from Vortex Streets," NACA Report 1191, 1954.
[17] Salari, K., and Knupp, P., "Code Verification by the Method of Manufactured Solutions," SAND 2000-1444, Sandia National Laboratories, 2000.
[18] Schmitt, V. and Charpin, F. "Pressure Distributions on the Onera-M6-Wing at Transonic Mach Numbers," Experimental Data Base for Computer Program Assessment. Report of the Fluid Dynamics Panel Working Group 04, AGARD AR 138, May 1979.
[19] Spalart, P.R. and Allmaras, S.R., "A One-Equation Turbulent Model for Aerodynamic Flows," *La Recherche Aerospatiale*, No. 1, 1994, pp. 5-21.
[20] Shu, C.-W., "Essentially Non-Oscillatory and Weighted Essentially Non-Oscillatory Schemes for Hyperbolic Conservation Laws," ICASE Report No. 97-65, November 1997.
[21] Visbal, M., and Gaitonde, D., "On the Use of Higher-Order Finite-Difference Schemes on Curvilinear and Deforming Meshes," *Journal of Computational Physics*, Vol. 181, 2002, pp. 155.
[22] Wilcox, D. C., *Turbulence Modeling for CFD*, 2nd Edition, DCW Industries, 1998.
[23] Woodward, P., and Colella, P., "The Numerical Simulation of Two-Dimensional Fluid Flow with Strong Shocks," *Journal of Computational Physics,* Vol. 54, 1984, pp. 115-173.
[24] Yang, J.-Y., Perng, Y.-C., and Yen, R.-H., "Implicit Weighted Nonoscillatory Schemes for Compressible Navier-Stokes Equations," *AIAA Journal* Vol. 39, No. 11, 2001, pp. 2082-2900.